Available online at www.sciencedirect.com
SCIENCE DIRECT®
International Journal of Heat and Fluid Flow 24 (2003) 223–235
International Journal of HEAT AND FLUID FLOW
www.elsevier.com/locate/ijhff

Coupled liquid film and solidified layer growth with impinging supercooled droplets and Joule heating

G.F. Naterer *

Department of Mechanical and Industrial Engineering, University of Manitoba, 15 Gillson Street, Winnipeg, Manitoba, Canada R3T 2N2

Received 29 January 2002; accepted 1 July 2002

Abstract

Phase change heat transfer with incoming supercooled droplets on heated curved surfaces is examined. The processes of rime ice, transition and combined rime/glaze ice conditions are modelled. In the analysis, heat conduction equations in the ice and unfrozen water layers are solved simultaneously with the mass balance, including incoming droplets. Energy input from the heated boundary (due to electrical heat generation) affects the growth of the glaze film thickness and associated liquid runback along the ice surface. Validation of the predictive model is carried out through comparisons with experimental data [Lu et al., A semi-empirical icing model for an energized power line, Internal Report, Department of Mechanical and Industrial Engineering, University of Manitoba, Winnipeg, Canada, 1999; Mass of ice accretion from freezing rain simulations, Proceedings, 8th IWAIS, Reykjavik, Iceland, 1998] involving ice buildup on heated, non-rotating circular conductors. Close agreement is achieved between the predicted ice growth and the measured data. Additional effects of cable radius, Joule heating rate and surface curvature are presented. The heat transfer model is shown to correctly approach the dry growth limit, based on mass conservation alone, under appropriate thermal conditions when the surface heating rate is diminished sufficiently. As a result, a single formulation is provided over the entire range of rime, transition and combined rime/glaze ice conditions, including the simultaneous growth of unfrozen water and ice layers.

1. Introduction

Phase change heat transfer with glaze ice is encountered in various engineering technologies. Glaze ice occurs under certain thermodynamic conditions near the equilibrium phase change temperature (i.e. 0 °C for water). Upon their release of latent heat by freezing, impinging droplets on an ice surface may heat the surface sufficiently to generate an unfrozen water layer with runback along the ice surface (called glaze ice). This process creates a three-phase problem (Naterer, 2002a) with a moving solid/liquid interface between the ice and the glaze film, and another moving liquid/air interface between the glaze film and the external air flow with droplets. Unlike glaze ice, the formation of rime ice only involves mass conservation since droplets are assumed to solidify immediately upon impact on the ice surface. In this article, heat transfer processes are examined for glaze ice, particularly the simultaneous coupling of solid and liquid growth rates when surface heat input (called Joule heating) is applied.

Examples of engineering problems involving glaze ice are icing of aircraft, power transmission lines, telecommunication towers and other structures. In the case of power lines, predictive models can be used as design tools in maintaining a reliable power supply during harsh weather conditions, such as freezing rain storms. Another example is helicopter icing, which can block the intake air and adversely affect cooling of the engine. The burning fuel within an aircraft engine produces intense heat, which is partly expelled through the exhaust of the engine. Since the remaining heat must be removed to prevent overheating, helicopter engines are air cooled by outside air. Under icing conditions, this outside air with supercooled droplets is forced into the engine compartment through openings on its front side or a separate intake cooling bay. These surfaces are often heated for ice prevention. The intake air is routed by baffles over various engine components to absorb/remove the

* Tel.: +1-204-474-9804; fax: +1-204-275-7507.
E-mail address: natererg@cc.umanitoba.ca (G.F. Naterer).

0142-727X/03/$ - see front matter © 2002 Elsevier Science Inc. All rights reserved.
doi:10.1016/S0142-727X(02)00195-9

Nomenclature

b	unfrozen water thickness
B	ice thickness
c_a, c_w	specific heats
E	collection efficiency ($E = 1$)
g_1, g_2, g_3	metric coefficients
G	liquid water content
h	convection coefficient
k	thermal conductivity
L	latent heat of fusion
N	view factor
q	heat flux (per unit area)
Q	heat input (per unit length)
r	local recovery factor
R	cable radius, or resistance
t	time
u_1, u_2, u_3	curvilinear coordinates
V	air velocity (magnitude)

Greeks

χ	reduction factor
ρ	density

Subscripts

a	ambient (air)
conv	convection
d	droplet
f	freezing point
i	ice
k	kinetic energy
l	latent heat
s	surface
w	water, transition to glaze ice

engine heat. This cooling air inflow encounters considerable drag forces (called cooling drag), particularly with iced surfaces. Reducing the cooling drag can lower the energy costs by improving the overall fuel efficiency. Also, operating the engine of the aircraft at higher than its design temperature can cause excessive oil and fuel consumption, loss of power, engine damage (i.e. warping of valves, pistons, rings) and possibly detonation. As a result, ice formation and blockage at any stage of these cooling flow processes should be reduced or eliminated. In this helicopter example, fully understanding the physical processes leading to glaze ice, particularly when surface heating is applied beneath the ice layer, is a key aspect of preventing the aircraft ice problems.

A thermodynamic analysis by Messinger (1953) identified the primary heat flows which contribute to a glaze ice formation. A comprehensive review of mathematical models of both rime ice and glaze ice is given by Poots (1996). Under certain atmospheric conditions (i.e. ambient temperatures below about −5 °C with unheated surfaces; Poots, 1996), rime ice accretion can be accurately predicted by Goodwin et al.'s model (1982). Both heat and mass balances must be considered during the transition from rime ice to glaze ice (Myers and Hammond, 1999), while consideration of entropy can further enhance the efficiency and accuracy of the phase change computations (Naterer, 2001). Tracking of the unknown positions of the solid/liquid and liquid/air interfaces is a key difficulty in the analysis of icing problems. These moving boundary problems involve heat conduction in the unfrozen water and ice layers, as well as non-linear energy balances at the phase interfaces.

The incoming droplets contribute significantly to the interfacial energy balances. The processes of droplet impact and deposition have been examined by Aziz and Chandra (2000) in applications involving spray coating and materials processing. Lee and Bragg (1999) present an experimental study involving large incoming droplets on iced aircraft surfaces. Al-Khalil et al. (1993) adopt a specified distribution of droplet impingement rate for aircraft icing predictions. Further experimental data involving freezing rain (droplet diameters of about 1 mm) and icing of power transmission lines has been presented by Lu et al. (1998). This data was used to confirm the accuracy of Goodwin's model over a range of atmospheric conditions. An extension of Goodwin's model to glaze ice predictions was presented by Naterer et al. (1999). The dynamics of incoming droplets at the ice/air (rime) or unfrozen water/air (glaze) interfaces is largely responsible for the final shape and mass of ice.

Spatially averaged equations can be used to predict the external multiphase flow with droplets (i.e. Banerjee and Chan, 1980). Since analytical solutions of multiphase flows are generally limited to 1-D domains, detailed modelling often requires a numerical discretization. A finite element model of multiphase flow with droplets and icing was presented by Naterer (2002b). Morphogenetic modelling of power line icing was presented by Szilder et al. (2001). Icing of power lines can produce undesirable galloping caused by combined ice and wind loads (Desai et al., 1996). Numerical analysis of solid/liquid phase change in these ice problems requires modelling of the interfacial heat balance, and potentially entropy for accelerated solution convergence (Naterer, 2000).

Despite these advances, it is not well understood how the coupled growth of solid and unfrozen water layers occurs in the presence of surface heating beneath the solidified layer. This surface heat input (called Joule

heating) affects the energy balance at the solid/liquid interface. Also, it reduces the temperature difference between the conductor/ice interface and the ice/water interface, thereby reducing the relative significance of heat conduction through the ice. In this article, predictive models based on previous studies by Messinger (1953), Myers and Hammond (1999), Myers (2001, 2002), and Poots (1996) are developed for icing processes over a range of surface heating rates. This Joule heating represents a boundary condition at the conductor/ice interface with practical importance in thermal de-icing technology.

This article differs from previous work (i.e., Myers and Hammond, 1999; Poots, 1996) in certain ways. A modified treatment of the droplet kinetic energy (boundary condition) is presented for extensions to large droplets with relatively low incoming velocities (icing of power lines). A surface view factor is documented for droplet capturing on curved surfaces. Also, corrections for surface curvature are described through a method of flux tubes. Furthermore, a reduction factor is developed for problems involving Joule heating. These predictive models are validated through comparisons with experimental data involving ice buildup on circular, non-rotating, heated conductors.

2. Problem formulation

The current problem involves three-phase conditions, including multiphase flow with droplets, phase change and heat conduction in the ice and unfrozen water layers (Naterer, 2002a). Based on previous studies, i.e. Messinger (1953); Myers and Hammond (1999); Naterer et al. (1999), the following heat flux terms (per unit area; designated by q) contribute to the energy balances.

- $q_k = (EVG)V^2/2$; kinetic energy of impinging droplets
- $q_l = \rho L(\partial B/\partial t)$; release of latent heat of fusion
- $q_a = rhV^2/2c_p$; viscous heating (coefficients adopted as by Myers and Hammond, 1999)
- $q_f = -k(\partial T/\partial y)$; rate of heat conduction through the ice or unfrozen water layer
- $q_d = EVGc_w(T_w - T_a)$; cooling by impingement of incoming supercooled droplets
- $q_{conv} = h(T - T_a)$; convective heat loss (based on Nusselt correlation; Makkonen, 1984)

The meaning of individual variables is outlined in the nomenclature and illustrated in Fig. 1(a) and (b). The following assumptions will be adopted in the upcoming analysis: (i) negligible effects of sublimation, turbulence, radiation, splashback of droplets and gravity-driven downflow of unfrozen water, (ii) temperature of the impinging droplets equals the ambient air temperature and (iii) constant thermophysical properties and convection coefficient.

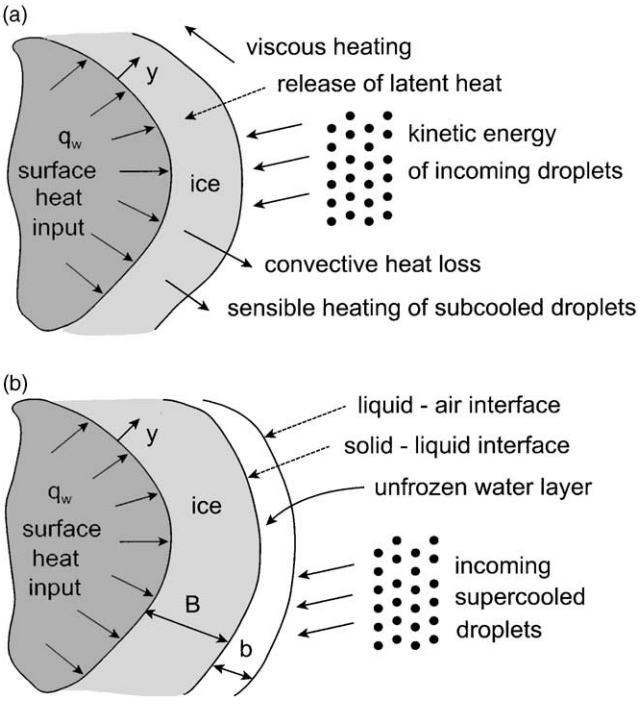

Fig. 1. Schematic of (a) rime ice ($t < t_w$) and (b) glaze ice ($t \geqslant t_w$).

Initially, rime (dry) ice accumulates on the surface in accordance with the following mass balance,

$$\rho_i \frac{\partial B}{\partial t} = EVGN \tag{1}$$

where $N = \int dx_p / \int dx$ represents a view factor for the projection of the curved surface in the direction of the droplet influx. The notations dx_p and dx refer to the projected and actual distances along the curved surface. For a planar surface, $N = 1$, but for other curved surfaces such as a circular conductor, the view factor is essential since the projected width of a circular conductor is twice the radius (not the entire circumference). Thus, $N = 1/\pi$ for a circular conductor. Then, solving Eq. (1), subject to $B = 0$ initially,

$$B = \left(\frac{EVGN}{\rho_i}\right)t \tag{2}$$

Although some previous studies group together the E and N factors into a single collection efficiency, it should be noted that these variables are independent. The collection efficiency, E, is defined as the ratio of impinging droplet mass flux, on the upstream side of the surface, to the mass influx that would occur on the surface if the droplets were not deflected by the air stream. On the other hand, N is a purely geometrical factor which accounts for the inability of incoming droplets to directly reach an obstructed side of the surface (i.e. back of the cylinder).

During the period of rime ice growth, latent heat from the incoming solidified droplets (in conjunction with other heat modes) is released at the phase interface. Over time, this heat transfer may raise the ice surface temperature sufficiently to sustain an unfrozen water layer with liquid runback along the ice surface. At the point of transition to glaze ice, Eq. (2) yields the following ice thickness:

$$B_w = \left(\frac{EVGN}{\rho_i}\right) t_w \tag{3}$$

where the subscript w denotes the onset to an unfrozen water film. Beyond this point, ice and unfrozen water typically co-exist and accumulate simultaneously over time.

In this section, two types of thermal boundary conditions (specified temperature; specified heat flux) are considered. The theoretical model for the first type of boundary condition (specified temperature) follows from Myers and Hammond (1999), and Poots (1996), except for certain changes required for applications to icing of ground-based structures such as power lines. This flow regime involves larger droplets and much smaller air velocities than conditions typically encountered during in-flight icing of aircraft. As a result, the treatment of droplet kinetic energy is different. Also, the second type of boundary condition (specified heat flux) involves modifying the formulation after using a new reduction factor. Furthermore, corrections for surface curvature and appropriate initial conditions are considered. An upcoming Section 4 will show that a useful contribution of this article becomes the experimental validation of these theoretical models.

2.1. Boundary condition: specified surface temperature

The time taken for an incremental growth in ice thickness is expected to be much smaller than the time taken for heat to be fully conducted through this newly formed layer. It is approximated that the layer grows sufficiently slowly that heat losses/gains at the phase interface are fully conducted throughout the solid. Then, heat conduction within the ice, as well as unfrozen water layers, is approximated to be quasi-steady (note: bounds described by Myers and Hammond, 1999). Laplace's equation is adopted, while the moving phase interface imposes a time varying boundary condition. The governing heat equation in the ice becomes

$$\frac{\partial^2 T_i}{\partial y^2} = 0 \tag{4}$$

subject to a boundary condition of $T_i = T_s$ at $y = 0$ and an interfacial condition of $T_i = T_f$ (phase change temperature) at $y = B$. Solving Eq. (4) subject to the boundary conditions,

$$T_i(y) = \left(\frac{T_f - T_s}{B}\right) y + T_s \tag{5}$$

This represents a quasi-steady result since the ice thickness, B, varies with time.

In an analogous manner for the unfrozen water layer,

$$\frac{\partial^2 T_w}{\partial y^2} = 0 \tag{6}$$

subject to $T(B) = T_f$ at $y = B$. An energy balance at the liquid/air interface ($y = B + b$) yields the following interfacial constraint,

$$k_w \left.\frac{dT_w}{dy}\right|_{B+b} + \frac{rhV^2}{2c_a} = h\left(T_w|_{y=B+b} - T_a\right) + EVGc_w(T_f - T_a) \tag{7}$$

where the terms represent conduction through the unfrozen water layer (first term), viscous heating (second term; typically negligible at lower air speeds) and cooling by convection (third term) and the incoming supercooled droplets (fourth term). Evaporative cooling is neglected for these problems involving relatively low air velocities during icing of ground-based structures (i.e., power lines; as compared with aircraft icing).

The expression for heat conduction in Eq. (7) depends on the slope of the temperature profile in the unfrozen water layer. There exists a lack of relevant experimental data due to the difficulty of obtaining nonintrusive, reliable temperature measurements over such a small distance within the glaze film. As a result, it is often considered that the equilibrium freezing temperature ($T_f = 0$ °C) can be adopted within the glaze film (i.e., Messinger, 1953). This difficulty is particularly evident in the current studies involving large droplets (up to 1 mm diameter) in relation to the thickness of the unfrozen water layer. However, certain features of the temperature profile are expected to be encountered from a physical perspective. A positive slope appears possible at $y = B$ due to the release of latent heat of solidified droplets, in contrast to a negative slope, which entails liquid below the equilibrium freezing temperature (despite available sites for heterogeneous nucleation). On the other hand, a negative slope at $y = B + b$ yields a net heat outflow from the system, which sustains the growth of ice. A certain change of temperature slope may arise within the unfrozen water layer. However, since this unfrozen water temperature is expected to be very close to T_f, it will be assumed that a single slope of temperature can be adopted in the current analysis.

In certain cases, the incoming droplets can essentially occupy the entire layer of unfrozen water nearly instantaneously upon impact, thereby contacting the ice/water interface at T_f. In the last term of Eq. (7), a temperature difference of $(T_f - T_a)$ is used for the large droplet/low air speed regime (i.e., icing of ground-based structures such as power lines). However, small droplets

at high air speeds represent a different flow regime during aircraft icing (i.e., Myers and Hammond, 1999), thereby leading to different interactions with droplets in the unfrozen water layer. These physical assumptions emphasize the importance of experimental validation (to be carried out in Sections 3 and 4).

Solving Eq. (6), subject to the boundary conditions,

$$T_w(y) = T_f - \frac{C_2 - C_1(T_f - T_a)}{1 + C_1 b}(y - B) \tag{8}$$

where $b(t)$ is the unfrozen water layer thickness and

$$C_1 = \frac{h + EVGc_w}{k_w}; \quad C_2 = \frac{rhV^2}{2c_a k_w} \tag{9}$$

A quasi-steady temperature profile is obtained, whereby the slope of the water temperature profile varies with time since both $B(t)$ and $b(t)$ are time dependent in Eq. (8).

The remaining unknowns, $B(t)$ and $b(t)$, can be obtained by a simultaneous solution of the interfacial energy and mass balances. For the energy balance at $y = B$ (ice/water interface),

$$\rho_i L \frac{dB}{dt} + k_w \left.\frac{\partial T_w}{\partial y}\right|_B + \frac{1}{2} EV^3 G = k_i \left.\frac{\partial T_i}{\partial y}\right|_B \tag{10}$$

Substituting the temperature gradients based on Eqs. (5) and (8) into Eq. (10), and rearranging,

$$\frac{dB}{dt} = \frac{C_3}{B} + \frac{C_4}{1 + C_1 b} + C_5 \tag{11}$$

where

$$C_3 = \frac{k_i(T_f - T_s)}{\rho_i L}; \quad C_4 = \frac{k_w(C_2 - C_1(T_f - T_a))}{\rho_i L}; \quad C_5 = -\frac{EV^3 G}{2\rho_i L} \tag{12}$$

The relative contribution of droplet kinetic energy to the energy balance depends on the droplet size in relation to the thickness of the unfrozen water layer. For small droplets (i.e. diameter of the order of microns; aircraft icing), the kinetic energy contribution would likely arise at $y = B + b$ (water/air interface) since the droplet impinges at the top of the unfrozen liquid film. However, for larger droplets (i.e. diameter of the order of a millimeter; power line icing), the contribution would likely appear at $y = B$ (ice/water interface). In that case, each droplet arrives nearly instantaneously at the ice surface, while passing through the thin liquid film without losing appreciable energy at the top of the water/air interface. Sensitivity studies have shown that the predicted rate of ice buildup appears to be similar and nearly independent of whether the kinetic energy of droplets is imposed at the water/air interface or the ice/water interface. If the droplets are larger or within the same order of thickness as the unfrozen liquid layer, then they can essentially occupy the entire glaze film nearly instantaneously upon impact. Then, the kinetic energy is expected to be largely imparted on the ice/water interface. Although it is beyond the scope of this article, the droplet kinetic energy is distributed spatially throughout the layer as each droplet passes through the layer.

Furthermore, the interfacial mass balance at $y = B$ requires that

$$\rho_i \frac{dB}{dt} + \rho_w \frac{db}{dt} = EVGN \tag{13}$$

subject to $B = B_w$ at $t = t_w$ from Eq. (3) at the onset of glaze ice. The value of B_w can be obtained by setting $b \to 0$ and equating the resulting expression in Eq. (11) with the rime ice result in Eq. (1), i.e.

$$B_w = \frac{C_3}{EVGN/\rho_i - C_4 - C_5} \tag{14}$$

$$t_w = \left(\frac{\rho_i}{EVG}\right) B_w \tag{15}$$

This transition time, t_w, was derived based on solving only a mass balance, Eq. (1), during the period of rime ice, rather than a combined heat/mass balance. Experimental data is available over a wide range of freezing rain conditions (Lu et al., 1998). It gives evidence that rime ice growth can be accurately predicted from a mass balance alone (i.e. Eq. (1); Goodwin et al., 1982), without additional convection and viscous heating coefficients that introduce further empirical coefficients for flows over time-varying rime ice shapes.

As a result, the B_w value in Eq. (14) is used as an initial condition for Eq. (13). Then, the mass balance in Eq. (13) is integrated and solved in terms of $b(t)$ and $B(t)$, thereby yielding

$$b = C_6 t + C_7 B + C_8 \tag{16}$$

where

$$C_6 = \frac{EVGN}{\rho_w}; \quad C_7 = -\frac{\rho_i}{\rho_w}; \quad C_8 = \frac{\rho_i}{\rho_w} B_w - \frac{EVGN}{\rho_w} t_w \tag{17}$$

The result in Eq. (16) can now be substituted into Eq. (11) and subsequently solved for $B(t)$. In this way, Eqs. (11) and (13) are solved for $B(t)$ and $b(t)$ sequentially. Since the equations are non-linear, coupled differential equations, the solution will be obtained numerically (i.e. Runge–Kutta solver).

2.2. Boundary condition: specified wall heat flux

The second type of boundary condition consists of a specified heat flux at the wall (conductor/ice interface). This case arises frequently in practical applications, such as de-icing of aircraft, power lines and other structures. It can be examined by considering a heat balance across the entire liquid film, or alternatively, an interfacial energy balance at the solid/liquid interface (see

Appendix A). Performing an energy balance over the combined ice and unfrozen water layers,

$$q_w + q_l + q_a + q_k = q_{conv} + q_d \tag{18}$$

which represents a balance between all energy inflows (left side) and energy outflows (right side). Heat input from the wall, q_w, to the ice requires that the temperature within the wall is higher than the temperature of the wall in contact with the ice. On the other hand, the ice layer is assumed to stay below T_f to remain in the solid phase, while the ice/liquid interface is assumed to be at the equilibrium phase change temperature (i.e. 0 °C for water). As a result, the temperature gradient is negative within the wall (with respect to the positive y direction), and then becomes positive thereafter (in the ice up to the ice/liquid interface). The practical role of the wall heat flux is to raise the wall temperature sufficiently to reduce or prevent the ice buildup on the surface.

Substituting the appropriate heat flux terms into Eq. (18),

$$q_w + \rho_i L\frac{\partial B}{\partial t} + \frac{rhV^2}{2c_a} + \frac{1}{2}EV^3G = h\left(T_w|_{y=B+b} - T_a\right) + EVGc_w(T_w - T_a) \tag{19}$$

Using the temperature profile from Eq. (8), and rearranging in terms of previously defined coefficients from Eqs. (9) and (12), the following result is obtained:

$$\frac{\partial B}{\partial t} = -\frac{q_w}{\rho_i L} - \frac{C_1C_4b}{1 + C_1b} + C_5 - C_4 \tag{20}$$

The first term on the right side of Eq. (20) gives the energy input from the heated boundary. From its leading minus sign, it can be observed that the ice growth decreases when the wall heat input, q_w, is raised. It should be noted that Eq. (19) is re-arranged independently of Section 2 (i). The same parameters of C_1, C_4 and C_5 appear due to the same heat flows contributing to the energy balance. Also, the water film temperature can be used from Eq. (8) in Eq. (19) since heat conduction in the unfrozen water layer is subject to the same boundary conditions in both cases. However, the wall temperature, T_s, is not known for the constant heat flux case, so certain modifications will be required for this case.

The approach used earlier in Case (i) for the time of transition to glaze ice, Eq. (15), is not adopted for the case of a specified flux boundary condition. A modification of Eq. (15) is required to adapt the temperature difference in C_3 of Eq. (12) to accommodate the specified flux boundary condition. In particular, this temperature difference changes due to the continual heat input from the wall to the adjoining ice layer. On average, the reduced temperature difference can be represented by a reduction factor, χ, multiplied by the initial temperature difference in Eq. (12). This product is calculated to approximately yield the same heat conduction through the ice as would be achieved for the actual case with a specified wall flux.

In practice, the uniform wall flux can be achieved by resistive type heating with electrical heat generation internally within the wall (to be called the additional heat source; Joule heating). This heat input leads to sensible heating, i.e., a change of surface temperature, T_s, above some initial/reference value. Consider the following two cases: (i) change of temperature without the additional heat source and (ii) change of temperature with the heat source. An energy balance at the wall/ice interface can be constructed for each case. These balances include heat conduction (Q_{cond}) and wall heating (Q_w), which can be expressed in terms of the latent heat release (Q_l), cooling (Q_d) and kinetic energy (Q_k) of incoming droplets. Dividing the equations for Cases (i) and (ii) yields a ratio of temperature differences, which approximates the aforementioned reduction factor, χ, i.e.,

$$\chi \equiv \frac{T_f - T_{s,h}}{T_f - T_s} = \frac{Q_{cond}}{Q_{cond} + Q_w + Q_l + Q_k - Q_d} \tag{21}$$

so that Eq. (12) becomes

$$C_3 = \frac{k_i\chi(T_f - T_s)}{\rho_i L} \tag{22}$$

In Eq. (21), the subscript h refers to the heated surface (associated with the specified flux boundary condition). The latter two terms, Q_k and Q_d, are usually much smaller than the other heat flows in typical problems involving icing of structures (i.e. negative denominator would not be observed).

Representative values of $k(T_f - T_s)$ (described further in Section 2.4 involving T_s) and the heat input per unit depth are used for the conduction and heat source terms, respectively. These closure relations provide the correct physical trends for the variations of χ. For example, as the wall heat input (Q_w) increases, then χ decreases in Eq. (21) so that C_3 is lower and the transition to glaze ice occurs earlier in Eq. (14). Conversely, if Q_w decreases, then χ and C_3 become larger so that glaze ice occurs later since less energy is added to the system. Also, from an energy balance for the constant wall temperature case, the denominator in Eq. (21) sums to Q_{cond}, thereby rendering $\chi \to 1$ in that case. Then, the same result for C_3 is obtained as earlier in Eq. (12) for the constant wall temperature case (as expected).

A main difficulty of this fixed wall flux case is the unique influence of this boundary condition on the nature of the conjugate problem between the wall and the ice. Consider the positive y-direction beginning at the wall ($y = 0$), together with wall heat input, q_w. There is a negative temperature gradient on the wall side; otherwise, a higher magnitude of q_w would lead to more cooling (not the intention of Joule heating). Also, there must be a positive temperature gradient (i.e., increasing

temperature in the increasing y direction) on the ice side of the wall; otherwise, the temperature would exceed T_f and cause melting, thereby removing the ice. The unique difficulty of the Neumann boundary condition (as compared with the Dirichlet or Robin type; Myers and Hammond, 1999) is maintaining a constant gradient in the wall, while allowing the temperature of the wall/ice interface to change over time. The current approach based on the reduction factor was found to be an effective method, while providing reasonable agreement with experimental data (to be discussed in Section 4).

In the problem formulation, the understanding of gravity-driven downflow of unfrozen water in the x-direction (tangent to the ice surface; see Fig. 1) should be elucidated. The focus and scope of this article involves the mass of ice buildup, rather than the shape of ice buildup. The gravity-driven downflow is considered to have a larger impact on the ice shape. A detailed investigation of ice shape has been presented elsewhere (Naterer, 2002b). In the present article, the unfrozen layer thickness, b, is assumed to be constant in the x-direction. Its variation in the x-direction due to gravity-driven downflow, i.e. $b(x)$, was investigated earlier (Naterer et al., 1999). But its inclusion did not significantly affect the successfully predicted rates of ice buildup. When the water thickness, b, is assumed to be constant, this means that the streamwise gradient of fluid enthalpy in the unfrozen layer is considered to be much smaller than thermal gradients normal to the phase interface (y-direction).

2.3. Corrections for surface curvature

Under certain conditions, heat conduction through the ice can be appreciably affected by surface curvature. For general curvilinear coordinates, the mutually orthogonal coordinates, u_1, u_2 and u_3, can be related to cartesian coordinates, x, y and z, using the chain rule of calculus, i.e.,

$$\mathrm{d}u_i = \frac{\partial u_i}{\partial x}\,\mathrm{d}x + \frac{\partial u_i}{\partial y}\,\mathrm{d}y + \frac{\partial u_i}{\partial z}\,\mathrm{d}z \tag{23}$$

where $i = 1$, 2 and 3. Metric coefficients, called g_1, g_2 and g_3, are based on the form of the leading coefficients in Eq. (23), i.e.

$$g_i = \left(\frac{\partial x}{\partial u_i}\right)^2 + \left(\frac{\partial y}{\partial u_i}\right)^2 + \left(\frac{\partial z}{\partial u_i}\right)^2 \tag{24}$$

Using these definitions, it can be shown that an element of arclength, ds, where

$$(\mathrm{d}s)^2 = (\mathrm{d}x)^2 + (\mathrm{d}y)^2 + (\mathrm{d}z)^2 \tag{25}$$

can be converted to curvilinear coordinates by

$$\mathrm{d}s_i = \sqrt{g_i}\,\mathrm{d}u_i \tag{26}$$

The result in Eq. (26) shows that the $\sqrt{g_i}$ values are scale factors involved in the transformation from cartesian to curvilinear coordinates. Based on Eq. (26),

$$\mathrm{d}A_1 = \mathrm{d}s_2\,\mathrm{d}s_3 = \sqrt{g_2 g_3}\,\mathrm{d}u_2\,\mathrm{d}u_3 \tag{27}$$

and similarly for dA_2 and dA_3, where dA refers to an area element.

Throughout the previous analysis, surface curvature was considered in the droplet mass influx (through the view factor, N), but not the thermal resistance to heat conduction in the ice. For example, the denominator, B, in Eq. (11) represents the geometric part of the thermal resistance for a planar layer. For a curved ice surface, it does not account for a varying area available to heat transfer in the direction of the heat flow. The following analysis provides a *flux tube method* as a correction of the thermal resistance to accommodate heat conduction across a curved layer. A flux tube refers to a region bounded by heat flow lanes in general curvilinear coordinates.

Considering a flux tube in the u_1 direction, the thermal resistance, R_t, of the differential volume element in that direction is

$$d^3R_{t,1} = \frac{T - (T + \mathrm{d}T)}{Q_1} = \frac{-k(\mathrm{d}T/\mathrm{d}s_1)\,\mathrm{d}s_1}{-k(\mathrm{d}T/\mathrm{d}s_1)\,\mathrm{d}A} = \frac{\mathrm{d}s_1}{k\mathrm{d}A_1} \tag{28}$$

The differentials ds_1 and dA_1 refer to the normal distance and cross-sectional area encountered in the path of the heat conduction. Substituting Eqs. (26) and (27) into Eq. (28),

$$d^3R_{t,1} = \frac{\mathrm{d}s_1}{k\mathrm{d}A_1} = \frac{1}{k}\left(\frac{g_1\,\mathrm{d}u_1}{\sqrt{g}\,\mathrm{d}u_2\,\mathrm{d}u_3}\right) \tag{29}$$

where $\sqrt{g} = \sqrt{g_1 g_2 g_3}$. When all flux tubes are assembled in parallel, the total thermal resistance to heat conduction through the ice layer can be obtained. Integrating Eq. (29),

$$\frac{1}{R_t} = \int_{u_2}\int_{u_3} \frac{k\,\mathrm{d}u_2\,\mathrm{d}u_3}{\int_a^b g_1/\sqrt{g}\,\mathrm{d}u_1} \tag{30}$$

where R_t represents the total resistance due to heat conduction through the curved layer of ice.

These results can now be used as a correction of thermal resistances for a planar layer. In particular, the unit resistance (denominator) in Eq. (11), B, can be replaced by a unit resistance (area times R_t), given by $R_{t,u}$, inferred from Eq. (30), i.e.,

$$R_{t,u} = \frac{\int_{u_2}\int_{u_3}\sqrt{g_2 g_3}\,\mathrm{d}u_2\,\mathrm{d}u_3}{\int_{u_2}\int_{u_3}\mathrm{d}u_2\,\mathrm{d}u_3/(\int_a^b g_1/\sqrt{g}\,\mathrm{d}u_1)} \tag{31}$$

The function obtained by Eq. (31), based on the curvature of the surface, can be used as a correction of B. The numerator in Eq. (31) represents the area, A_1, available to heat flow in the calculation of the unit

resistance. For example, in a cylindrical geometry, the curvilinear coordinates adopted in Eq. (31) are $u_1 = r$ (radial), $u_2 = \theta$ (angular) and $u_3 = z$ (axial). Then, the conduction term on the right side of Eq. (11) can be modified for cylindrical coordinates, i.e.,

$$\frac{C_3}{B} \to \frac{C_3}{R\ln((R+B)/R)} \tag{32}$$

where R (without a subscript) refers to the radius of the circular (uniced) conductor. It can be readily verified that Eq. (31) yields the proper thermal resistances for common geometries, such as a plane layer or a cylindrical annulus.

In the previous analysis, the individual terms in Eq. (19) represent energy fluxes (per unit area). In consideration of surface curvature, these fluxes are multiplied by appropriate surface areas to yield the total energy flows at the inflow and outflow boundaries of the selected control volume. Although the temperature profile in Eq. (5) does not represent all coordinate systems, its corresponding heat flux (temperature difference divided by thermal resistance) can be generalized to those coordinates. This extension, based on the metric coefficients, can be carried out through the generalized thermal resistance in Eq. (31). Heat conduction occurs between the inner and outer edges of the growing ice layer.

Due to the actual irregular shape (i.e. when not completely cylindrical), the region cannot be generally bounded entirely by a single coordinate system. Solving the planar heat conduction equation, Eq. (4), is viewed to provide better geometric flexibility when applying the method to other curved surfaces. For example, a curved surface can be more effectively analyzed numerically with piecewise linear solutions, as compared with piecewise cylindrical solutions in the x-direction (parallel to the surface). Also, even with icing of cylindrical cables, the shape of the ice buildup is often unsymmetrical and not perfectly cylindrical. As a result, the current approximate analysis uses a geometric correction to the planar heat flux, based on Eq. (31), for irregular geometries, rather than cylindrical coordinates.

2.4. Initial conditions

In addition to the boundary conditions, an initial condition must be specified before the onset of ice. For example, based on the following initial energy balance between internal heat generation (left side) and convective heat losses (right side) prior to the onset of ice buildup on a circular conductor (per unit length),

$$\dot{q}(\pi R^2) = (2\pi R)h(T_s - T_a) \tag{33}$$

which can be re-arranged to yield the following initial condition:

$$T_s = T_a + \frac{\dot{q}R}{2h} \tag{34}$$

where $\dot{q}$ is the volumetric heat generation rate within a circular conductor. This result can be applied as the initial surface temperature prior to ice buildup if T_s remains at or below T_f; otherwise, the icing process is assumed to not be initiated. The heated surface is assumed to melt any incoming droplets whenever its surface temperature exceeds the phase change temperature (i.e., 0 °C for water).

3. Experimental studies

Experimental data has been used for assessment and validation of the icing predictions (Lu et al., 1998, 1999). Reproducing freezing rain in a laboratory setting is a difficult task, especially since large droplets emitted from a spray system require a large distance of travel in a surrounding cold air stream to reach thermal equilibrium with the air at a sub-zero temperature. As a result, performing the experiments in an outdoor setting provides certain practical benefits of realistically simulating freezing rain. In the present context, outdoor spray nozzles were positioned far enough away from various test specimens to simulate freezing rain essentially naturally. A weight scale and microscope were used to measure the size spectrum of the water droplets. The mean volume diameter of droplets was approximately 1 mm, which fairly represents freezing rain in atmospheric icing of ground-based structures. However, this droplet size is generally larger than sizes encountered in aircraft icing applications. For example, typical in-flight icing of helicopters would occur at −30 °C at 60 m/s with a 0.02 mm typical droplet size.

A fan delivers cold outside air at sub-zero temperatures past a horizontal, circular conductor placed perpendicular to the air stream (see Fig. 2). Droplets are sprayed from the nozzles (located behind the fan) onto each test specimen. The ejected droplets are pre-cooled to leave the nozzles at slightly above 0 °C to prevent freezing in the supply tubes. In order to study the effects of Joule heating, the inner steel core of the circular test specimen was replaced by a resistive type heater. The

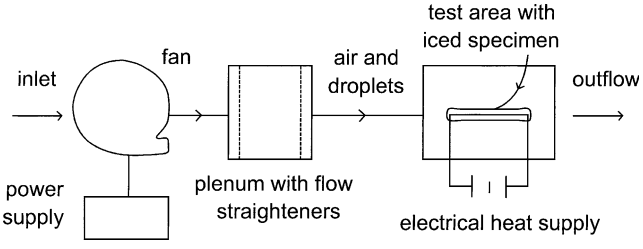

Fig. 2. Schematic of experimental apparatus.

amount of heat supplied to the heater rod was adjusted by altering the input voltage from the DC power source. A main quantity of interest in this study is the influence of surface heating on the mass and rate of ice growth. Plaster cast duplicates were used to determine the growth of ice by replicating the ice shapes at various points in time. Two methods were used and compared, namely (i) tracing out an area (and thus mass) around the cast sample and (ii) measuring a displaced liquid volume (and thus mass) caused by the sample when it is submerged inside a liquid container. Once an area or volume of ice was obtained, multiplication by the appropriate density yielded the mass of ice. Then, this ice mass was converted to an equivalent thickness of ice, based on a uniform radial thickness which yields the same mass as that actually observed.

Based on these techniques, the ice thickness can be measured, but not the thickness of the unfrozen water layer (due to surface runoff). The ice thickness represents the position of the interface between the ice and the unfrozen water. It would be difficult to individually collect the unfrozen water layer when the plaster cast samples are made, due to uncontrolled mixing of surface runoff with other incoming droplets (not directly contacting the ice surface). However, the difference between the measured ice growth and the total droplet influx on the surface indicates the corresponding mass of unfrozen water. This total droplet influx represents the maximum capturing of droplets by the surface (i.e. dry growth limit).

The air speed produced by the fan was measured by an anemometer. Also, the horizontal and vertical components of precipitation were measured with two precipitators. It is worthwhile to elaborate on the experimental difficulties of matching velocity components of the air and droplets when studies of large droplets (mean diameter of about 1 mm) at relatively low air speeds are considered. Since a large distance of travel is required for the droplets to reach thermal equilibrium with the air, ejecting the droplets horizontally into the air stream is impractical for certain reasons. The large droplets would fall under gravity before reaching the test specimen. Otherwise, they would have to be ejected into the horizontal air stream with a velocity far greater than the low speeds typically encountered in ground-based icing problems. As a result, the droplets were sprayed along a trajectory which was viewed to give a sufficient distance of travel to reach thermal equilibrium with the air, while reaching the test specimen as uniformly as possible.

The sources of experimental errors and uncertainties were viewed to be mainly caused by the measurement of the precipitation arriving on the test specimen. The air velocities, precipitation and air temperature were monitored at half-hour intervals. In view of the previous discussion regarding a long distance of travel required for droplets to reach thermal equilibrium, this requirement becomes a limitation and uncertainty in terms of the actual mass of droplets arriving on the specimen. Comparable experiments were performed over various time intervals, and the ice mass and precipitation rates were monitored separately to assess the experimental uncertainties. It was estimated that the experimental data reported (Lu et al., 1998, 1999), including ice thickness and precipitation rate, was accurate within about $\pm 10\%$. Specific experiments were performed more than once to confirm the repeatability of the measured data. Additional details of the experimental setup are fully described by Lu et al. (1998, 1999).

4. Results and discussion

Computed and experimental results will be presented for ice buildup on heated circular conductors. The practical importance of these studies is its application to current loading for thermal de-icing of overhead power transmission lines. During ice buildup, the incoming droplets are partially solidified, due to runback of unfrozen water along the growing ice surface. The following three cases of surface heating rate (per unit length of cable), Q, will be considered in this article. The liquid water content, G, cable radius, R, and freestream velocity and temperature, V and T_a, respectively, are outlined for each case in the following list:

- Case 1: $Q = 46$ W/m, $G = 0.00078$ kg/m^3, $T_a = 267.5$ K, $V = 5$ m/s, $R = 1.43$ cm
- Case 2: $Q = 20$ W/m, $G = 0.00056$ kg/m^3, $T_a = 270.3$ K, $V = 6$ m/s, $R = 1.05$ cm
- Case 3: $Q = 25$ W/m, $G = 0.00064$ kg/m^3, $T_a = 268$ K, $V = 5$ m/s, $R = 1.43$ cm

The results obtained for these three cases are illustrated in Figs. 3–7. Thermophysical properties of air, ice and water are given in Appendix B.

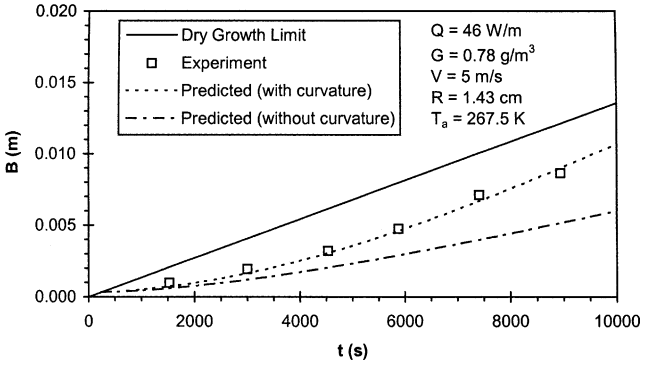

Fig. 3. Predicted and measured ice thickness (Case 1).

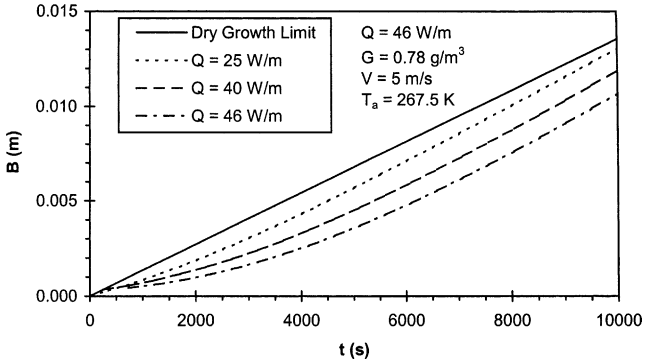

Fig. 4. Effects of surface heating rate (Case 1).

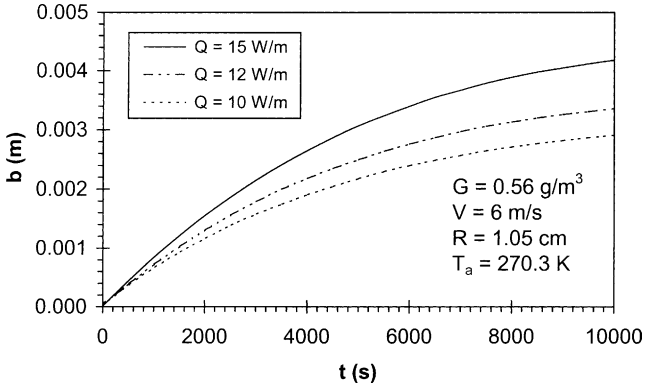

Fig. 5. Transient growth of the unfrozen liquid layer (Case 2).

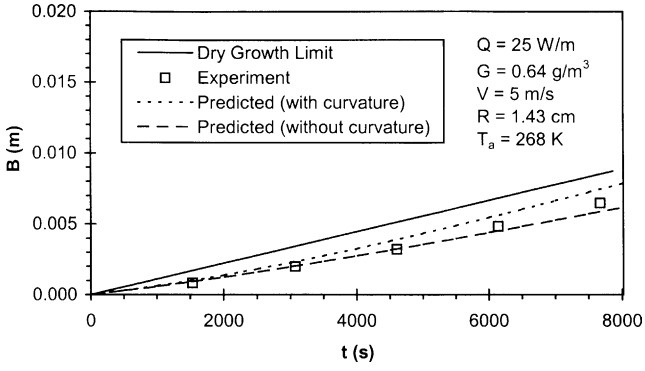

Fig. 6. Predicted and measured ice thickness (Case 3).

The main validated quantities are the mass and rates of ice buildup on the heated surface with respect to time. For icing of circular cables, an equivalent ice thickness, B, is defined as the uniformly radial ice thickness having the same mass of ice as the actual observed ice accretion. Previous experimental studies for unheated, non-rotating conductors indicate that the ratio of equivalent ice thickness to time should remain nearly constant (Goodwin's model; Lu et al., 1998). Goodwin's model will be referenced frequently here for comparison purposes, and it will be called the dry growth limit, since it is

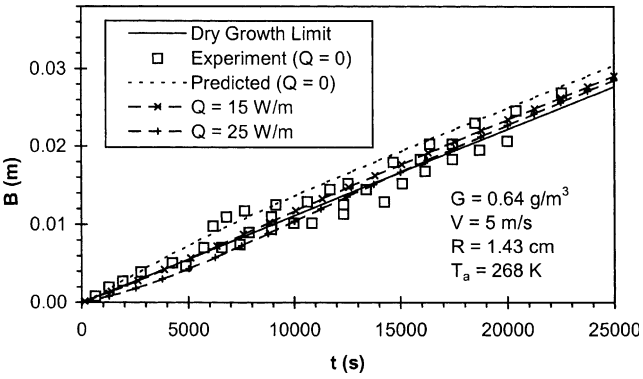

Fig. 7. Asymptotic trends of low surface heating (Case 3).

based on a conservation of mass alone. The dry growth limit is reached when all incoming droplets are assumed to freeze immediately upon impact on the surface (i.e. not requiring thermal analysis). Goodwin's model has been well validated experimentally for rime and glaze ice (Lu et al., 1998). The reduction factor, χ, will be used for the previously mentioned three cases involving Joule heating, when finding the transition time to glaze ice. In particular, the coefficient C_3 (based on χ) is calculated in Eq. (22) and later used to find the glaze ice transition time in Eq. (15). The solution changes from Eq. (2) to Eq. (20) once the transition to glaze ice occurs.

In the upcoming figures, the predicted ice thickness will be compared with experimental data (depicted by boxed data points) and the dry growth limit. Dry growth can occur in a variety of possible ways. For example, if the ambient air temperature is sufficiently low, then the heat released by the impinging supercooled droplets upon freezing would be insufficient to sustain an unfrozen water layer along the ice surface. If there is a close proximity between the computed results and the dry growth limit, this indicates that relatively low surface heating and/or liquid water content do not add enough energy to appreciably reduce the accumulation of ice (as compared with dry growth). It will be shown that the present analysis approaches the dry growth limit when the surface heating is diminished sufficiently (as expected).

The rate of ice growth in Case 1 is shown in Fig. 3 when relatively high Joule heating is applied. Good agreement is achieved between the predicted and measured results when surface curvature is considered. Surface runoff of unfrozen water along the surface leads to slower ice growth than the dry growth limit. Although this surface runoff is not directly predicted by the current thermal analysis, it can be inferred from the difference between the dry growth limit and the combined ice and unfrozen water mass retained on the surface (i.e. predicted by the b plus B variations over time). In addition to the surface heat input, latent heat is released at the phase interface by incoming droplets,

thereby contributing to the surface runoff of unfrozen water. In Fig. 3, it can be observed that surface curvature effects are sufficiently important to warrant their consideration in the thermal analysis. Without considering the area changes for heat conduction through the ice (i.e. without curvature; discussed in Section 2.3), the rate of ice growth is under-predicted due to the extra heat flux arising from the under-predicted area of the growing ice boundary.

Transition from rime ice to glaze ice occurs when the net energy input to the ice surface (including the release of latent heat of impinging solidified droplets) raises the surface temperature of the ice sufficiently to sustain an unfrozen water layer on the surface. In Fig. 3, it can be observed that the computed results (dashed line) intersect the dry growth limit (solid line) slightly ahead of the origin of the B–t axes. Before this intersection point, the ice thickness grows linearly in time along the dry growth limit during rime ice growth. During this period, droplets are solidified upon impact on the surface without sufficient energy added to sustain an unfrozen layer.

Transition to glaze ice is predicted at the intersection point, beyond which the ice growth rate diminishes due to surface runoff. Although the transition point to glaze ice was not specifically measured, it may be viewed from a backward extrapolation from the experimental data to its intersection with the dry growth limit. The predicted transition time in Fig. 3 appears consistent with the trend indicated by the backward extrapolation of experimental data. Although there is a range of time (Fig. 3) corresponding to this backward extrapolation, the predicted transition time establishes the proper trends afterwards. For example, in Fig. 3, if the transition time was largely over-predicted, then the entire dashed curve would be translated upwards, thereby showing a corresponding disagreement with the experimental data points at later times.

The effects of Joule heating rate are illustrated in Fig. 4. In these sensitivity studies, the indicated parameter is independently modified and all other remaining parameters are kept constant (as specified for Case 1). The results in Fig. 4 for $Q = 46$ W/m agree well with experimental data shown earlier in Fig. 3 (measured for $Q = 46$ W/m). As expected, the rate of ice growth increases when the surface heating rate is lowered. As incoming droplets impact on the surface and unfrozen water flows along the ice surface, a higher net rate of heat loss from the ice interface leads to more ice accumulation when the wall heating is lowered.

In Case 2, certain parameters are lowered, including the Joule heating rate (Q), liquid water content (G) and cable radius (R). In Fig. 5, the predicted growth of the unfrozen water layer along the ice surface is depicted over time for Case 2. The results generally indicate that this glaze film approaches a certain thickness over time. It has been validated that the decreasing slope of glaze film growth over time in Fig. 5, particularly at the end time shown, occurs coincidentally and closely with the slope of ice growth approaching the dry growth slope. This is consistent with the mass conservation between incoming droplets, ice and unfrozen water, since the lower rate of unfrozen water growth comes at the expense of higher growth of ice. It appears that a quasi-steady balance occurs between the heat released from the advancing ice interface and the heat losses from the edge of the glaze film. When the change of unfrozen water thickness with time becomes small, then the incoming droplets mainly contribute to an increase of ice mass. A balance between the mass of incoming droplets and the growing mass of ice becomes analogous to the dry growth limit based on Goodwin et al.'s model (1982). It can be observed that the slopes of rime ice (dry growth limit) and glaze ice growth nearly match each other in Fig. 4 at large times.

The unfrozen water layer leads to surface runoff from the ice surface. In this article, the mass and energy balances at the solid/liquid interface determine the proportion of the droplet influx which solidifies on impact on the ice surface. The remaining proportion represents the non-solidified mass, such as surface runoff of unfrozen water and droplets. This proportion corresponds to the difference between the dry growth limit (no surface runoff) and the actual predicted ice growth curve. Although not directly predicted in the current results, droplet bounce-back or splash-back can be accommodated in the current formulation if appropriate experimental correlations for E (collection efficiency) are available for these processes. When using the collection efficiency, this parameter includes impinging droplets that bounce or splash, but are later collected in the unfrozen water layer, since they stay on the ice surface.

Other sensitivity studies (not shown here) confirm that the glaze film thickness decreases when the ambient air temperature is lowered. As expected, this trend indicates that the glaze film thickness would eventually disappear with sufficiently low ambient temperatures. Once the supercooled droplet temperature is sufficiently low (typically below about -5 °C for unheated conductors; Poots, 1996), its release of latent heat upon impact and solidification is lower than the net heat loss from the freezing droplet. As a result, the droplet solidifies immediately upon impact, without producing an unfrozen water layer. In Fig. 5, the unfrozen water thickness decreases when Q is lowered. Due to higher net heat losses from the ice/water interface, more liquid is solidified. In view of the overall mass balance of incoming droplets, a smaller glaze film thickness leads to a larger growth in ice mass (as depicted in Fig. 4 for Case 1).

Case 3 is examined in Figs. 6 and 7. In Fig. 6, the Joule heating rate is $Q = 25$ W/m and the liquid water content is $G = 0.00064$ kg/m^3. Fair agreement is achieved between the predicted and measured results in

this case. When considered in view of the range of experimental uncertainty (discussed in Section 3), reasonable predictions are obtained with or without surface curvature corrections. It seems that the lower surface heat input leads to less sensitivity to heat conduction effects through the surface curvature correction (as compared to Case 1). There is a closer proximity to the dry growth limit, when thermal effects are diminished as a higher proportion of droplets are solidified on impact. Also, it should be noted that only the rate of ice mass buildup is shown in Fig. 6, not the shape of ice. The experimental studies have shown that different ice shapes may occur during glaze icing of cables, including top/bottom asymmetry with locally planar behaviour.

An important validation test for any glaze ice analysis is to check that the ice growth approaches the proper limit when the wall heating rate diminishes. This limit occurs when all droplets are solidified immediately upon impact and a mass balance alone yields Goodwin et al.'s model (1982). When the Joule heating rate (Q) is lowered sufficiently, the heat transfer predictions should not exceed the range of measured data centered about Goodwin's model (dry growth limit). Fig. 7 shows this correct trend. When Q is lowered, the predicted results stay within the range of experimental data (boxed data points) obtained for unheated conductors ($Q = 0$). The experimental data in Fig. 7 represents ice growth on unheated conductors over a range of droplet impingement rates, cable sizes and air temperatures and velocities. In particular, this range encompasses $-25\ ^\circ\mathrm{C} < T_a < -1\ ^\circ\mathrm{C}$ (ambient air temperature), $0 < V < 10$ (m/s) (wind speed), $0.8 < d < 1.4$ (mm) (droplet diameter) and $0.65 < R < 2.2$ (cm) (cable radius). Due to this range of conditions, more than one data point may be shown at nearly the same time. These data points lie within a close proximity of Goodwin's model (solid line).

Some measured data points and predicted results exceed the dry growth limit. In Goodwin's model, only droplets arriving on the surface in the projected distance into the wind direction are captured by the surface. However, some droplets can adhere at the sides of the iced conductor, both from the freestream flow adjacent to the conductor, as well as droplets deflected around the conductor from the front side of the conductor. The main purpose of examining this data is to verify that the predictive model exhibits the correct limiting behaviour as $Q \to 0$. The predicted results show that the limiting cases stay within the upper bound of experimental data for unheated conductors. The current model successfully captures a range of ice conditions including rime ice (dry growth limit; low surface heating rates), transition and combined rime/glaze ice conditions.

Although this study, as well as similar previous studies, have attempted to derive analytical models for ice buildup on curved surfaces, the sensitivity and dependence of all of these models on various empirical coefficients should not be overlooked. Some examples of empirical coefficients include the convection coefficient (typically accurate within $\pm 25\%$) and the collection efficiency. Despite these limitations, the goal of these studies is viewed more in terms of the capabilities of predicting the correct physical trends with reasonable accuracy. For instance, the relative influences of surface heating rate and conductor size have been described in this article. As a result, deeper physical insight has been gathered to attempt to reduce the empirical nature of ice protection systems.

5. Conclusions

In this article, a time dependent model is developed to predict the simultaneous growth of ice and unfrozen water on heated curved surfaces. The predictive model includes heat conduction (through the ice and unfrozen water layers), convection and incoming droplets, which absorb sensible heat from the ice surface, release latent heat and impart kinetic energy upon impact. Transition occurs from rime ice to glaze ice with surface runoff due to unfrozen water along the ice surface. The heat conduction equations in the ice and the unfrozen water layer are solved simultaneously with the mass balance of incoming droplets and ice accumulation. The predictive model is applied to ice buildup on an electrically heated cable. Reasonable agreement is achieved between predicted results and experimental data. Furthermore, the heat transfer model is shown to correctly approach the dry growth limit when the surface heating is lowered sufficiently. In this way, a new unified model is presented over the range of conditions including rime ice, transition and combined rime/glaze ice growth with Joule heating.

Acknowledgements

The assistance, insight and/or support provided by Dr. N. Popplewell, Mr. M. Lu (University of Manitoba; UM), Mr. W. Barrett (UM; deceased 23 October 2001), Mr. G. Venn and Dr. G. Richardson (GKN Westland Helicopters Ltd), Mr. J. Chan (Manitoba Hydro), and Dr. T. Myers (Cranfield University), are appreciated. Also, financial support from the Natural Sciences and Engineering Research Council of Canada is gratefully acknowledged.

Appendix A. Boundary condition: constant wall heat flux

The governing equations involve conduction in the ice, i.e.

$$\frac{\partial^2 T_i}{\partial y^2} = 0 \tag{A.1}$$

subject to $T_i = T_f$ at $y = B$ (ice/liquid interface) and $dT/dy = q_w/k$ at $y = 0$. Solving Eq. (A.1) subject to the boundary conditions,

$$T_i(y) = T_f + \frac{q_w}{k}(B - y) \tag{A.2}$$

The governing, boundary and interfacial conditions in the unfrozen water layer remain the same as derived earlier, i.e. Eq. (10), except the evaluation of conduction in the ice. Based on Eq. (A.2),

$$\frac{dB}{dt} = \widetilde{C}_3 + \frac{C_4}{1 + C_1 b} + C_5 \tag{A.3}$$

where

$$\widetilde{C}_3 = -\frac{q_w}{\rho_i L} \tag{A.4}$$

Also, the following coefficient is defined by

$$C_9 = \widetilde{C}_3 + C_5 + \frac{C_6}{C_7} \tag{A.5}$$

Other constants remain the same as defined earlier in Eqs. (9), (12) and (17).

In the present work, the solution of Eq. (A.3) is obtained by a numerical ODE solver (using *Maple V*). However, a closed-form solution of Eq. (A.3) can be obtained. In obtaining this solution, Eq. (16) is substituted into Eq. (A.3) and a change of variables is performed, i.e.

$$M = -\frac{C_4}{C_6 t + B} \tag{A.6}$$

The third term in Eq. (A.3) is replaced by this single new variable.

After changing all variables appropriately, and solving the simplified differential equation subject to $B = B_w$ (or $M = M_w$) at $t = t_w$, we obtain the final result that

$$B = \left(\frac{C_6 \rho_w}{\rho_i}\right) t - \frac{1}{C_7}\left(C_8 + \frac{1}{C_1} + \frac{C_4}{C_1 M}\right) \tag{A.7}$$

where M is defined implicitly as follows:

$$\ln\left[\frac{(C_9 - M)M_w}{M(C_9 - M_w)}\right] + \frac{C_9}{M} - \frac{C_9}{M_w} = -\frac{C_1 C_7 C_9^2}{C_4}(t - t_w) \tag{A.8}$$

Thus, at any instant of time, the value of M is obtained from Eq. (A.8) and substituted into Eq. (A.7) to find the ice thickness, B, at that time.

Appendix B. Thermophysical properties

For ice, $\rho_i = 917$ kg/m^3, $c_i = 2030$ J/kg K and $k_i = 1.8$ W/m K. For water, $\rho_w = 1000$ kg/m^3, $c_w = 4220$ J/kg K, $k_w = 0.57$ W/m K and $L = 3.3 \times 10^5$ J/kg. For air, $c_a = 1014$ J/kg K, $k_a = 0.024$ W/m K and $v_a = 1.3 \times 10^{-5}$ m^2/s. Other remaining parameters and coefficients have been adopted from previous studies by Myers and Hammond (1999) and Makkonen (1984).

References

Al-Khalil, K.M., Keith Jr., T.G., De Witt, K.J., 1993. New concept in runback water modeling for anti-iced aircraft surface. AIAA Journal of Aircraft 30 (1), 41–49.

Aziz, S.D., Chandra, S., 2000. Impact, recoil and splashing of molten metal droplets. International Journal of Heat and Mass Transfer 43, 2841–2857.

Banerjee, S., Chan, A., 1980. Separated flow models—I. Analysis of the time averaged and local instantaneous formulations. International Journal of Multiphase Flow 6, 1–24.

Desai, Y.M., Yu, P., Shah, A.H., Popplewell, N., 1996. Perturbation-based finite element analyses of transmission line galloping. Journal of Sound and Vibration 191, 469–489.

Goodwin, E.J., Mozer, J.D., Di Gioia, A.M., Power, B.A., 1982. Predicting ice and snow loads for transmission lines, Proceedings, 1st IWAIS, 1982, pp. 267–273.

Lee, S., Bragg, M.B., 1999. An experimental investigation of simulated large droplet ice shapes on airfoil aerodynamics. Journal of Aircraft 36 (5), 844–850.

Lu, M.L., Popplewell, N., Shah, A., Barrett, W., Au, A., 1998. Mass of ice accretion from freezing rain simulations, Proceedings, 8th IWAIS, Reykjavik, Iceland, 1998.

Lu, M., Popplewell, N., Shah, A.H., Deng, H., Naterer, G.F., 1999. A semi-empirical icing model for an energized power line, Internal Report, Department of Mechanical and Industrial Engineering, University of Manitoba, Winnipeg, Canada, 1999.

Makkonen, L., 1984. Modeling of ice accretion on wires. Journal of Climate and Applied Meteorology 23, 929–939.

Messinger, B.L., 1953. Equilibrium temperature of an unheated icing surface as a function of air speed. Journal of the Aeronautical Sciences 20, 29–42.

Myers, T.G., 2001. An extension to the messinger model for aircraft icing. AIAA Journal 39 (4), 211–218.

Myers, T.G., 2002. Slowly accreting ice due to supercooled water impacting on a cold surface. Physics of Fluids 14 (1), 240–256.

Myers, T.G., Hammond, D.W., 1999. Ice and water film growth from incoming supercooled droplets. International Journal of Heat and Mass Transfer 42, 2233–2242.

Naterer, G.F., 2000. Predictive entropy based correction of phase change computations with fluid flow—Part 1: Second law formulation. Numerical Heat Transfer B 37 (4), 393–414.

Naterer, G.F., 2001. Applying heat—entropy analogies with experimental study of interface tracking in phase change heat transfer. International Journal of Heat and Mass Transfer 44 (15), 2917–2932.

Naterer, G.F., 2002a. Heat Transfer in Single and Multiphase Systems. CRC Press, Boca Raton, FL.

Naterer, G.F., 2002b. Multiphase flow with impinging droplets and airstream interaction at a moving gas/solid interface. International Journal of Multiphase Flow 28 (3), 451–477.

Naterer, G.F., Deng, H., Popplewell, N., 1999. Predicting and reducing glaze ice accretion on electric power lines with joule heating: theory and experiments. CSME Transactions 23 (1A), 51–70.

Poots, G., 1996. Ice and Snow Accretion on Structures. John Wiley and Sons Inc, New York.

Szilder, K., Lozowski, E., Farzaneh, M., 2001. Morphogenetic modelling of wet ice accretions on transmission lines as a result of freezing rain. International Journal of Offshore and Polar Engineering 11 (1), 16–22.